Chapter 1

ANISOTROPY OF ASSEMBLIES OF DENSELY PACKED FERROMAGNETIC NANOPARTICLES EMBEDDED IN CARBON NANOTUBES

Serghej L. Prischepa[1,2,*], Alexander L. Danilyuk[1] and Ivan V. Komissarov[1,2]

[1]Belarusian State University of Informatics and Radioelectronics, Minsk, Belarus

[2]National Research Nuclear University (MEPhI), Moscow, Russia

ABSTRACT

We report the results related to the impact of magnetic anisotropy on the properties of a new type of nanocomposite consisting of ferromagnetic nanoparticles (NP) embedded in carbon nanotubes (CNT). Samples were synthesized by chemical vapor deposition. We found that for low NP concentration, NPs are intercalated mainly inside CNTs and the extended magnetic order, up to hundreds of nanometers, presents in samples. It is shown by analyzing the correlation functions of the

[*] Corresponding Author's E-mail: prischepa@bsuir.by.

magnetic anisotropy axes that the extended order is not simply due to random anisotropy but is associated with the coherent magnetic anisotropy. With increasing temperature, the extended magnetic order is lost, the exchange coupling becomes stronger, but the coherent anisotropy still occurs. The magnetic coupling between NPs distant from each other for tens and hundreds of nanometers could occur via the RKKY interaction. The magnetic relaxation measurements confirmed the importance of the magnetic anisotropy at low temperatures. For the first time, we have been able to analyze the relaxation data using the temperature dependence of the magnetic anisotropy. We demonstrate further that, when each nanotube contains only one ferromagnetic NP, the magnetoelastic anisotropy plays an important role and leads to the formation of densely packed array of magnetically isolated nanoparticles.

Keywords: carbon nanotubes, correlation function of the magnetic anisotropy axes, law of the approach to magnetic saturation, magnetic relaxation, magnetoelastic anisotropy

INTRODUCTION

Magnetic nanostructured composites (nanocomposites) consisting of densely packed ferromagnetic nanoparticles (NPs) embedded in matrix material represent an increased performance of devices together with a sustained interest in understanding their fundamental properties. Improved coercivity H_C, saturation magnetization M_S and magnetic anisotropy have been already reported for different kinds of magnetic nanocomposites [1–3]. These magnetic properties are determined by the properties of NPs embedded into matrix material. Single domain NPs are characterized by single magnetic moment with a direction adjusted by local anisotropy. Their stability of the magnetization with time depends on the relation between thermal energy and total anisotropy energy of the NP, KV_{NP}, where K is the effective anisotropy energy density and V_{NP} is the volume of NP. With a noticeable decrease in V_{NP}, the contribution of K to this product should increase in order to maintain thermal stability. The K is generally the superposition of magnetocrystalline (K_{MC}), shape (K_S) and magnetoelastic (K_{ME}) energies. If K_{MC} does not exceed $10^4 – 10^5$ J/m^3 for

3d metals (Fe, Ni, Co), the K_S, which is proportional to the square of the saturation magnetization M_S^2, could reach values of 10^6 J/m^3. Finally, in nanostructured materials plastic deformations are constrained by surfaces and interfaces. As a result, these materials may have significant elastic stresses. The contribution of K_{ME} becomes decisive if elastic stresses of the order of 1-10 GPa are reached. In addition, cooperative effects between ferromagnetic NPs and matrix material could be of interest both from the fundamental and practical point of view. Such kind of interaction is determined by many factors, like arrangement of NPs in the matrix, electrophysical and magnetic properties of the matrix material, as well as NP/matrix interfaces. These factors, in turn, depend on the technology which is applied for the NPs embedding into the matrix. Different approaches are currently used to fabricate matrix dispersed NPs. Among others it is worth mentioning co-precipitation, thermal decomposition, emulsion methods [4], co-evaporation [5], electrochemical processes [6] and chemical vapor deposition (CVD) [7]. The material of the matrix could also vary in a wide range, covering polymers [5], silica [4], porous alumina [8], carbon nanotubes (CNT) [6, 9], etc.

Among all possibilities, CNT-based magnetic nanocomposites are of special interest. Such material presents a porous conducting discontinuous medium. Ferromagnetic NPs can be localized inside or outside of the nanotube inner channels. The aspect ratio of inclusions can vary in a wide range, from 1 to approximately 100, indicating formation of objects with variable morphology, from nanoparticles to nanowires. Number of NPs inside nanotubes can be varied between 1 and many, depending on the fabrication technology.

The role of the CNT in the interparticle interaction is of great importance. Despite porosity, the CNT matrix usually is a well-conducting object. Therefore, this conducting medium can provide indirect exchange coupling (IEC) between ferromagnetic nanoparticles [10, 11] with long-range character [12, 13]. Moreover, NPs inside CNTs can experience significant stresses which reflects on the magnetic anisotropy. All this is reflected in the particular interparticle interaction, creating peculiarities in the interplay between the magnetic anisotropy and exchange coupling [14,

15], which could be studied within the random anisotropy model (RAM) [14, 16, 17]. The contribution of the magnetic anisotropy in the total energy of the system can be so large that it exceeds the dipole interaction. This leads to the formation of ensemble of closely packed magnetically isolated nanoparticles which is important for magnetic data storage. In addition, large values of magnetic anisotropy could influence the magnetization relaxation at low temperatures.

CORRELATION FUNCTIONS OF THE MAGNETIC ANISOTROPY AXES

The mechanisms of the interparticle interaction as well as the magnetic anisotropy contribution can be studied using different methods. One of the most affordable is the investigation of isothermal magnetic hysteresis loops, $M(H)$. Such magnetostatic parameters like H_C, M_S, remanence M_{rem}, and their temperature dependencies can be obtained from the $M(H)$ results. Within such an approach it is possible to derive useful information regarding such magnetic properties of the studied materials like magnetization reversal mechanisms, type of magnetic anisotropy, etc [1, 18, 19]. The shape of the high field part of $M(H)$ curve could give additional important information about the interparticle interaction. Analyzing the law of the approach to magnetic saturation (LAS), it is possible to distinguish the cases of magnetically isolated and strongly interacting via exchange coupling NPs [20–23]. The approach towards magnetic saturation is of specific interest for CNT-based nanocomposites with ferromagnetic NPs because this part of the $M(H)$ curve is defined by general characteristics of a sample and does not contain metastable states [24]. However, the approach developed for the LAS in the past does not take account of possible matrix material contribution, which can significantly vary both the magnetic correlation lengths and the type of coupling between NPs embedded in the magnetic matrix. Even new

magnetically ordered states could be induced by peculiarities of interparticle interactions [25, 26].

Usually the exchange coupling between crystalline NPs can be considered when the inequality $R_c < R_f$ is fulfilled. Here R_c is the average radius of the NP and R_f is the exchange correlation length. The peculiarity of the exchange correlations depends on the dimensionality of the NP arrangement. For H far from H_{ex} (the exchange field) phenomenological LAS can be estimated as

$$\frac{\delta M(H)}{M_S} = \frac{M(H)-M_S}{M_S} \sim H^{-\alpha} \quad (1)$$

where the exponent α depends on the dimensionality d, $\alpha = (4-d)/2$ [16]. For example, for the three-dimensional (3D) case $\alpha = 1/2$, while for the two-dimensional (2D) interaction $\alpha = 1$. When $\alpha = 2$, it means that the magnetic anisotropy dominates. Usually this occurs at $H >> H_{ex}$. From Eq. (1) it follows that the analysis of the magnetization curve $M(H)$ in the region where $M \rightarrow M_S$ could give, in a relatively simple way, useful information about the dimensionality of the NPs interaction which, in turn, could be related to their arrangement. Indeed, many experimental works have been dedicated to such kind of study. In particular, 3D dimensionality was unambiguously established in different amorphous compounds [27] and nanostructured Fe and Ni materials [28].

2D dimensionality is a characteristic feature of thin films with thickness $d_f < R_f$ [29] and of nanocrystalline thick materials ($d_f >> R_f$), but with anisotropic ferromagnetic correlation lengths, $R_f^{||} \gg R_f^{\perp}$ [30]. Finally, a 1D system of exchange-coupled ferromagnetic NPs was reported for Fe nanowires embedded inside inner channels of CNTs [31]. In all these studies authors usually demonstrated, as the evidence of dimensionality, the $\delta M/M_s$ vs. $H^{-\alpha}$ plot only for a single exponent α. The obtained agreement between the experimental data and Eq. (1) with a single exponent α was used as the main argument, supporting a particular dimensionality.

On the other hand, for CNT based nanocomposites, such elaboration of the experimental data does not lead to the unambiguous statement about the actual dimensionality [14]. It should be noted that the simple relation (1) is not applicable in the range of magnetic fields comparable to the field of exchange interaction. However, usually the measurements of the LAS are carried out precisely when the condition $H \sim H_{ex}$ is met. Consequently, Eq. (1) is no longer valid, the contribution of the magnetic anisotropy becomes significant and a more general approach should be considered, in which the magnetic ordering is described by the correlation function $C(r)$ of the magnetic anisotropy axes in the real space [23]. This approach allows obtaining important information about the mechanism of magnetic interaction between NPs intercalated inside CNT: interplay between exchange coupling and magnetic anisotropy, role of the coherent anisotropy (CA) and its relation with the random anisotropy, and, finally, indication of the impact of the CNT medium on the interparticle interaction [32]. The expression for LAS in this case depends on the dimensionality of the system.

For 1D and 3D the general expression for LAS is [24]

$$\frac{\delta M(H)}{M_S} = \frac{1}{30}\left(\frac{H_{ra}}{H_{ex}}\right)^2 \left(\frac{H_{ex}}{H}\right)^{\frac{1}{2}} \int_0^\infty d^3x\, C(x) x^2 \exp\left[-x\left(\frac{H}{H_{ex}}\right)^{1/2}\right] \quad (2)$$

where H_{ra} is the random anisotropy field, the coordinate x is normalized to the R_a value, the length over which magnetic anisotropy axes are correlated.

For 2D the magnetization approaches saturation as [14]

$$\frac{\delta M(H)}{M_S} = \frac{1}{32}\left(\frac{H_{ra}}{H_{ex}}\right)^2 \left(\frac{H_{ex}}{H}\right)^{\frac{1}{2}} \int_0^\infty d^3x\, C(x) x^2 K_1\left[x\left(\frac{H}{H_{ex}}\right)^{\frac{1}{2}}\right], \quad (3)$$

where K_1 is the modified Hankel function.

The boundary conditions for the correlation function are

$$C(0) = 1, C(x \gg 1) \longrightarrow 0 \quad (4)$$

The analysis of the experimental data at $H \sim H_{ex}$ according to Eqs. (2) and (3) with boundary conditions (4) provide an explicit form of $C(x)$. Before performing these analysis it is necessary to establish the dimensionalty of the system. This can be done applying the law (1) to the experimental data.

It is worth noticing that in the above analysis the possible contribution of the CA is neglected. Taking account of the CA results in the modification of the LAS. In particular, such auxiliary quantities like the coherent anisotropy correlation length $\delta_{ca} \sim R_a (H_{ex}/H_{ca})^{1/2}$ and field $H_{sa} \equiv H_{ra}^4/H_{ex}^3$ are introduced in the theory [33]. The field of the CA can be evaluated from $C(x)$. In the presence of a field $H > H_{ca}$ in equations for correlation function one needs simply to replace external magnetic field H by $H + H_{ca}$ [33]. Thus the final expression for the LAS in the presence of both random and coherent anisotropy contributions is

$$\frac{\delta M(H)}{M_S} = \frac{1}{30}\left(\frac{H_{ra}}{H_{ex}}\right)^2 \left(\frac{H_{ex}}{H+H_{ca}}\right)^{\frac{1}{2}} \int_0^\infty d^3x\, C(x) x^2 \exp\left[-x\left(\frac{H+H_{ca}}{H_{ex}}\right)^{1/2}\right] \quad (5)$$

The explicit form of the correlation function is obtained by fitting the experimental data and estimating the Laplace integral

$$F_{3D}(p) = 4\pi \int_0^\infty dx \exp(-px) x^2 C(x) \quad (6)$$

The correlation function in the 2D case is obtained by fitting the experimental data within the Eq. (3) and applying the *K*-transform [34],

$$F_{2D}(p) = \int_0^\infty dx\, f(x)\, (px)^{1/2} K_1(px) \quad (7)$$

Note that the Eq. (3) can be rewritten in a form more convenient for the experimental data elaboration,

$$\frac{\beta}{p^2} = \left(\frac{H_{ra}}{H_{ex}}\right)^2 \frac{4\pi}{32 p^{\frac{3}{2}}} \int_0^\infty dx\, C(x) x^{\frac{3}{2}} (px)^{1/2} K_1(px) \quad (8)$$

With $p = (\frac{H}{H_{ex}})^{1/2}$ and β a constant determined by the slope of the dependence (1).

SAMPLES

Samples studied in this work were fabricated by two different methods. The first one was a floating catalyst chemical vapor depostion (FCCVD). Another one was based on the plasma enhanced CVD (PECVD) on flat substrate on which NPs of Co were preliminary deposited. In both approaches nanotubes were vertically aligned with the packing density $10^{10} – 10^{11}$ cm^{-2}. This quantity determined the density of arrangement of ferromagnetic nanoparticles.

FCCVD was applied for synthesis of vertically oriented densely packed CNTs with iron-based NPs located mainly inside inner channels. This was realized by using small concentration of ferrocene ($Fe(C_5H_5)_2$) as a catalyst [35]. In Figure 1a we show the scanning electron image (SEM) of one of the sample synthesized with ferrocene concentration C_F = 0.6wt%. Transmission electron microscopy (TEM) revealed that iron-based NPs are embedded inside CNTs. This result is presented in Figure 1b. The average distance between NPs located in one nanotube was usually about 100 nm, see Figure 1c. More details about samples preparation by FCCVD and their characterization can be found elsewhere [16, 17, 32].

The second approach is based on the growth of vertically oriented CNT array from fixed catalytic Co NPs preliminary deposited onto Si substrate. A SiO_2 layer of 8 nm thickness was first deposited onto Si(100) substrate. Then Co film of 5 nm thickness was deposited with an evaporation cell in an UHV chamber directly connected to the CVD reactor. Afterwards the substrate was transferred into the UHV CVD reactor, and the metal reduction and the formation of an array of Co NPs were performed by heating up to 973 K at a heat rate of 10 K/min under UHV followed by a final treatment at 973 K in a hydrogen/ammonia mixture at 15 mbar. These conditions were chosen to optimize the

formation of homogeneous distribution of NPs. Finally, the metal reduction and the formation of array of Co NPs were performed in thermally activated mixture of hydrogen and ammonia at 973K during 15 min. As a result, a reference sample consisting of an ensemble of Co NPs with an average diameter of 15±5 nm and $n_{NP} \approx 1.2\times10^{10}$ cm^{-2} was synthesized on the surface of SiO_2/Si substrate.

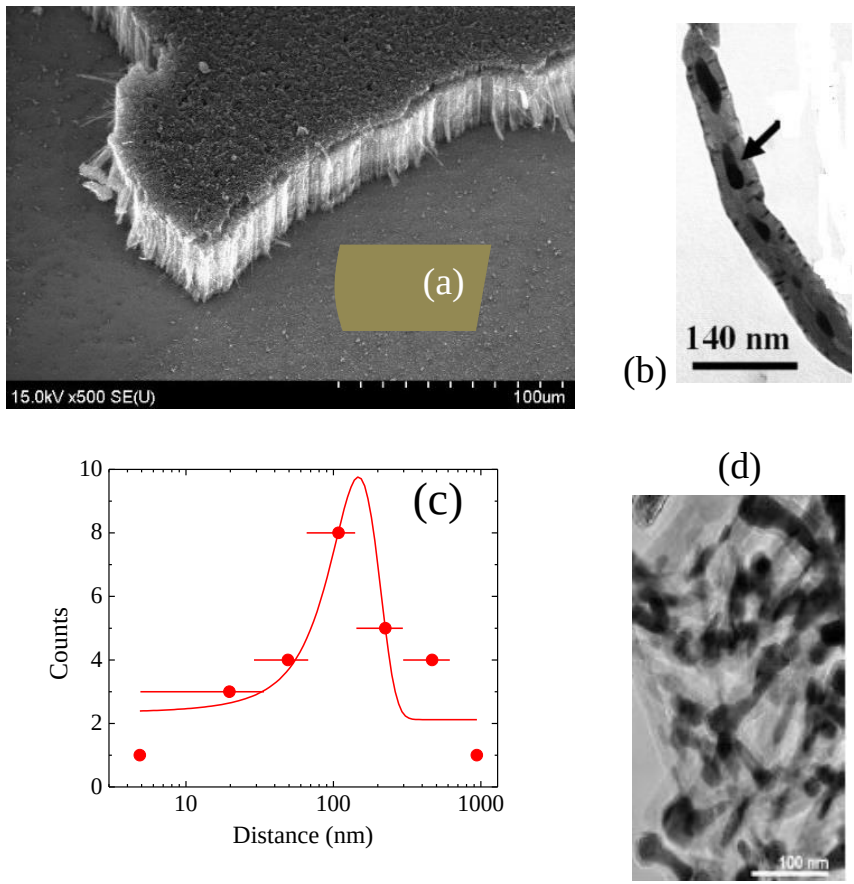

Figue 1. (a) SEM image of vertically oriented CNT array grwon by FCCVD on Si substrate; (b) TEM image of one CNT with ferromagnetic NPs inside (NP is marked by arrow); (c) Average distribution between adjacent NPs along one single nanotube; (d) TEM image of CNTs grown by PECVD with one ferromagnetic NP in each nanotube.

The process of PECVD was performed in the mixture of C_2H_2:H_2 = 20:80. In this case, vertically oriented array of CNTs is sytnthesized, each nanotube containes only one ferromagnetic NP located at the top, which is consistent with what is expected for plasma-activated process. The TEM image of such kind of sample is shown in Figure 1d. We emphasize that most of these Co NPs are elongated, as can be seen in Figure 1d, with the long axis oriented parallel to the nanotube axis. The diameter of these inclusions is restricted by the inner CNT channel (≈ 15 – 20 nm) and their aspect ratio is about 5, i.e., the NPs have a cylindrical-like shape. Such resulting Co morphology embedded on top of CNT underlines the importance of diffusion processes in/on the NP bulk/surface during the CNT growth. Crystalline structure of Co NPs consists of both cubic *fcc* and hexagonal *hcp* lattice as obtained from SAED study [36]. More details about fabrication of CNT with one ferromagnetic NP by PECVD can be found elsewhere [37-40].

CORRELATION FUNCTIONS OF MAGNETIC ANISOTROPY AXES OF FCCVD SAMPLES

In Figure 2 we analyze the high field part of $M(H)$ curves for sample synthesized by FCCVD with C_F = 0.6 wt.%. Data are presented for the temperature range 4-300 K according to the simplified Eq. (1) in order to determine possible dimensionality of the interparticle interaction. Magnetic field is oriented parallel to the CNT axes. In Figs. 2(a)-2(d) we show the correspondence of the experimental data to all possible exponents α in Eq. (1).

It follows from the result of Figure 2 that the dimensionality of the sample can not be determined unambiguously. The main result of this analysis is that at each T it is possible to find a certain range of H, in which one or another exponent α is valid. The situation could be clarified analyzing the width of the magnetic field range, ΔH_α, where the LAS (1) is

valid, for each α value and temperature. This result is presented in Figure 3.

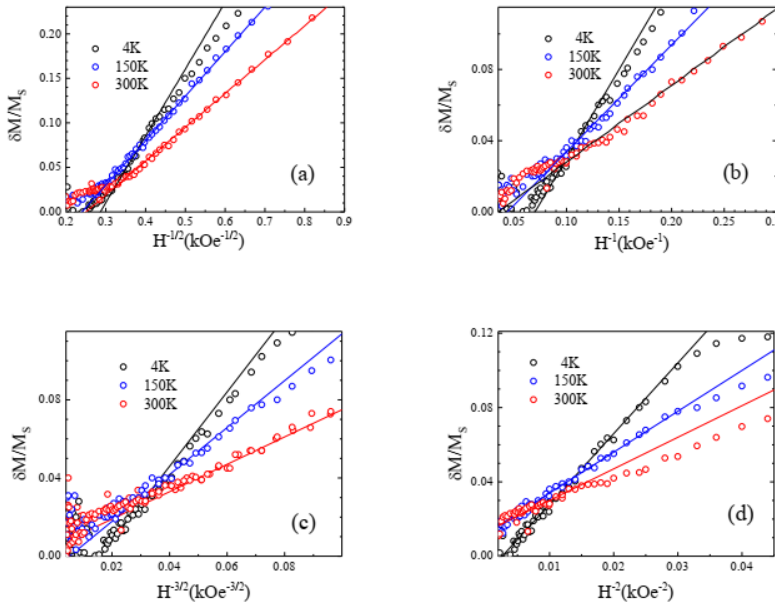

Figure 2. Analysis of LAS at different exponent α values according to Eq. (1) for sample synthesized with C_F = 0.6 wt.% by FCCVD. Data are for T = 4, 150 and 300K. (a) α = 1/2, (b) α = 1, (c) α = 3/2, (d) α = 2.

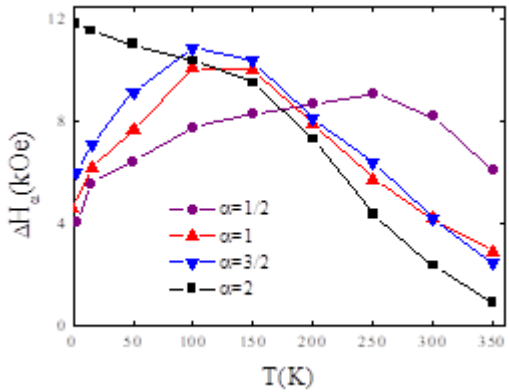

Figure 3. Temperature dependence of ΔH_α obtained from data of Figure 2.

It follows from Figure 3 that the values of ΔH_α vary significantly with the exponent α and T. For the temperature interval 2 – 50 K the widest range of ΔH_α corresponds to α = 2. For high temperatures, 200 K < T < 350 K, the exponent α = ½ gives the agreement with the experiment in the widest H range. At that interval ΔH_α for other exponents are absorbed by the dominant interval. Finally, for the intermediate temperatures, range between 100 K and 200 K, the ΔH_α values for α = 2, 3/2, and 1 are practically the same. Data of Figure 3 are typical for samples with NPs embedded inside CNTs [32]. It means that the dimensionality changes with temperature from mainly 0D at low T to mainly 3D at T > 200 K via the mixed state at which different dimensionalities are realized simulteneously.

The quantitative analysis of the experimental data was performed within the standard approach based on the RAM [14, 33, 35, 42, 43] and modified LAS [14, 24, 32, 35, 44-48]. Both these approaches are widely exploited for the analysis of the magnetic properties of amorphous, polycrystalline ferromagnets and CNT-based magnetic nanocomposites.

Within the RAM the local anisotropy field H_{ra} and the exchange field H_{ex} are expressed as

$$H_{ra} = \frac{2K}{M_S} \tag{9}$$

$$H_{ex} = \frac{2A}{M_S R_a^2} \tag{10}$$

The constant A is the constant of the exchange coupling. The values of H_{ra} and H_{ex} were evaluated according to the algorithm evolved earlier in [14]. R_a was assumed to be the half of the average diameter of CNT, $R_a \approx R_c \approx \emptyset_{CNT}/2 \approx 15$ nm. Finally, A was calculated as A = (3 – 5)×10^{-12} J×m^{-1}. As a result, we get H_{ra} = 3–6 kOe and H_{ex} = 2–5 kOe. These estimations imply that the values of the exchange field fall within, or are very close to, the range of the LAS. It means that well known simple models for the LAS, strictly speaking, cannot be applied for the quantitative experimental data interpretation, because they have asymptotic character, i.e., are valid only in the limits $H << H_{ex}$ and $H >> H_{ex}$ [16, 41].

In the considered case it is necessary to apply the approach, which operates for the intermediate fields, $H \approx H_{ex}$ [16, 24]. It means that, along with the exchange interaction both local random and coherent anisotropies should be considered [32, 33].

Therefore, we use the modified expression (5) for the LAS analysis. For the best fit procedure of the experimental data the Laplace integral (6) in the T range 2–150 K is close to p^{-3}. It means that, applying the boundary conditions (4) the correlation function is the Fermi-Dirac like

$$C_{0D}(x) = \frac{1}{1+\exp\left(\frac{x-x_{1/2}}{2}\right)} \tag{11}$$

where $x_{1/2}$ is a coordinate at which $C_{3D}\left(x_{1/2}\right) = 1/2$. This correlation function is shown in Figure 4 by solid line.

At high temperatures, $T > 200$ K, the Laplace integral was obtained as $F(p) = G\exp(-b/p)p^{-\gamma-1}$, where G, b and γ are constants. For such Laplace representation the correlation function is

$$C_{3D}(x) = x^{\left(\frac{\gamma}{2}\right)-2} b^{-1/2} J_{\gamma}\left[2(b(x+x_0))^{1/2}\right], \tag{12}$$

where J_{γ} is the γ-th order Bessel function of the first kind and x_0 is a constant. This correlation function is shown in Figure 4 by dashed line.

In the intermediate T interval (100 K < T <150 K) the experimental data can also be fitted with the Laplace integrals $F(p) \approx p^{-1}$ and $F(p) \approx p^{-2}$. The first Laplace integral leads to the correlation function

$$C_{2D}(x) = \frac{1}{x^2} \cdot \frac{1}{(x^2-a^2)^{\frac{1}{2}}} \left\{ \left[x + (x^2-a^2)^{\frac{1}{2}}\right]^{2m} + \left[x - (x^2-a^2)^{\frac{1}{2}}\right]^{2m} \right\}, x > a \tag{13}$$

where parameters a and m are determined from the fitting procedure. The second Laplace integral gives

$$C_{1D}(x) = \frac{1}{x} \tag{14}$$

The obtained correlation functions are depicted in Figure 4.

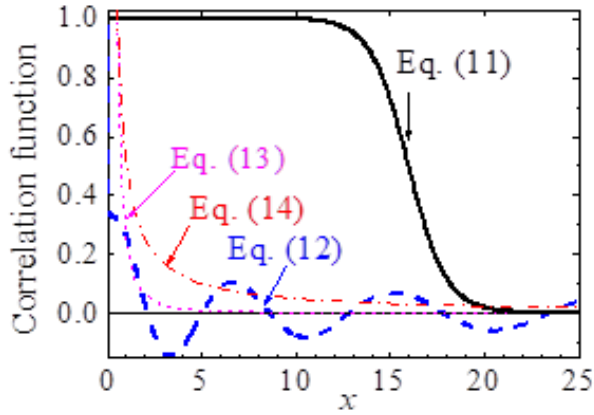

Figure 4. Correlation functions as obtained analyzing the experimental data.

The obtained correlation functions for 2D and 1D dimensionalities thus lead to the following general analytical expression for LAS

$$\frac{\delta M(H)}{M_S} = \frac{4\pi}{15}\left(\frac{H_{ra}}{H+H_{ca}}\right)^2\left[1 - exp\left(-\frac{H+H_{ca}}{H_{ex}}\right)^{1/2}\right]\left[1 + n \times \left(\frac{H+H_{ca}}{H_{ex}}\right)^{1/2}\right] \tag{15}$$

where the multiplier n is determined from the fitting procedure. In particular, we got that, for $\alpha = 1$ $n = 1$ and for $\alpha = 3/2$ $n = ½$.

The fitting procedure of the $M(H)$ data in parallel field revealed that the correlation function $C_{0D}(x)$ explains better the experiment at low temperatures. The result of the fitting procedure at $T = 4$ K is shown in Figure 5. In addition, the term of the coherent anisotropy is of great importance. Curve at Figure 5 is plotted with the following parameters: $H_{ex} = 3.8$ kOe, $H_{ra} = 4.0$ kOe, $H_{ca} = 3.5$ kOe. It should be emphasized that without H_{ca} term it was impossible to fit the experimental data. Correlations of the magnetic anisotropy axes in this case propagate up to

150–200 nm. This value is close to the mean distance between adjacent NPs embedded inside CNT, see Figure 1c. Such long-range correlations manifest the crucial role of the coherence anisotropy in the determination of the magnetic properties of CNT-based magnetic nanocomposite.

At high temperatures the $M(H)$ data are fitted better applying the $C_{3D}(x)$ correlation function. The result for T = 300 K is shown in Figure 5. Even in this case the fit of the experimental data excluding the mechanism of the coherent anisotropy was impossible. The obtained parameters were as follows, H_{ex} = 3.0 kOe, H_{ra} = 2.3 kOe, H_{ca} = 0.8 kOe.

In Figure 6 we plot the temperature dependence of the evaluated H_{ra} and H_{ca} fields. Shadow areas in Figure 6 mark regions where the mentioned correlation functions are valid. Despite the higher values of the H_{ca} for the $C_{0D}(x)$, the better agreement is reached for the $C_{3D}(x)$ at high T. This means that the crossover from low dimensionality to 3D occurs at temperatures around 200 K. The real H_{ca} value drop significantly due to thermal energy [49].

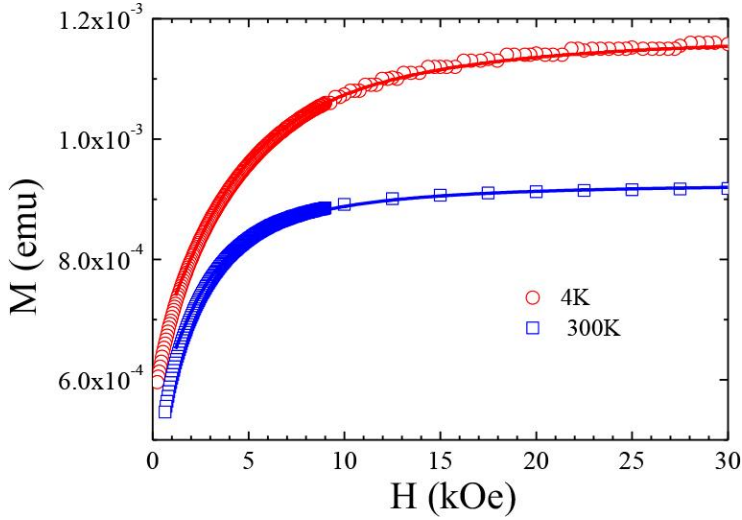

Figure 5. Analyses of LAS at T = 4 K and 300 K. Symbols are for the experiment, solid lines refer to the best fit procedure according to Eq. (15) (4 K) and Eq. (5) (300 K). For T = 4 K the correlation function was $C_{0D}(x)$, while for T = 300 K the correlation function $C_{3D}(x)$ resulted in the best agreement with the experiment.

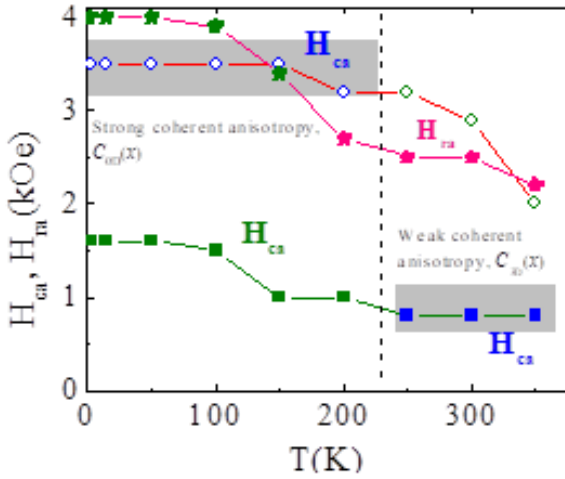

Figure 6. H_{ca} versus T for correlation functions according to the Eq. (11) (upper curve) and Eq. (12) (lower curve). H_{ra} versus T is the same for both functions.

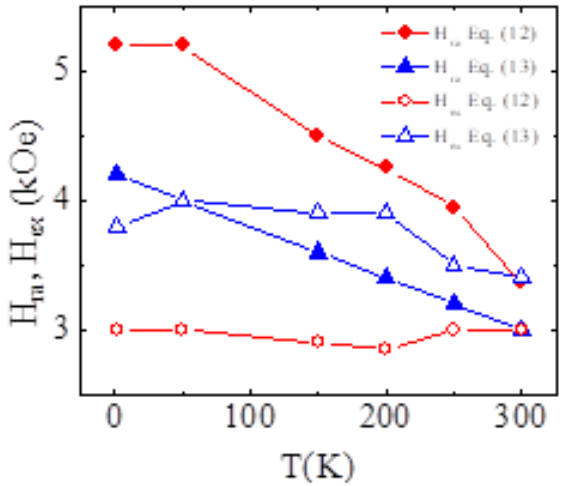

Figure 7. H_{ra} (closed symbols) and H_{ex} (open symbols) versus T extracted from the fitting procedure.

In Figure 7 we present the H_{ra} and H_{ex} versus T as obtained applying two correlation functions, in the 3D and 2D cases. It follows that at low T anisotropy dominates over the exchange interaction between NPs for both $C(x)$. At high T anisotropy still dominates for 3D case, whereas for 2D the

exchange interaction is stronger. The latter could be caused by short range character of the correlation function determined by Eq. (13).

The obtained manifestation of the importance of the coherent anisotropy underlines the extremely complex nature of the interparticle interaction via the CNT medium. The alignment of the CNTs also plays a crucial role in the observed long-range correlations of the magnetic anisotropy axes. When the alignment is destroyed, i.e., the oriented array of CNTs becomes a powder, the exponent α in LAS (1) is no longer equal to 2, and becomes equal to ½ [15].

On the other hand, even for strong impact of the coherent anisotropy, the exchange interaction is significant in the system with great (hundreds of nanometers) interparticle distance. Actually, the usual RAM cannot explain this fact. We should involve additional mechanism of indirect exchange coupling (IEC) via the conducting CNT medium. Actually, the peculiarity of the CNT-based nanocomposite is the conductivity of the CNT matrix. In ref. [13] the Rudermann-Kittel-Kasuya-Yosida (RKKY) interaction in single-walled semiconductor CNT with diameters of the order of 1 nm was considered. It was demonstrated that, due to spin-orbit interaction (SOI) [50] the IEC along the CNT axis could reach the value of 1 micrometer [13]. For such a large length of the IEC the constant of spin-orbit splitting equal to 6 meV and the Fermi level shift $\mu \sim 0.5$ eV are required [13, 51]. This significant shift of the Fermi level can be induced by any defects of the nanotubes or their doping [52, 53]. The large spin-orbit coupling was experimentally detected in CNTs [54]. It is reasonably supposed that defective conducting nanotubes investigated in this study could be a suitable environment for the indirect exchange interaction.

Based on the model developed by Klinovaja and Loss [13] we looked for the indications of the possibility of the long-range RKKY interaction in our samples. A theoretical model is based on the consideration of the properties of single-walled CNT (SWNT). The diameter of SWNT does not exceed few nanometers. Strictly speaking, our nanotubes do not fit the criterion of single-walled. However, we can assume with a very effective probability that the IEC occurs through one shell that could be the internal shell. Therefore, we considered for simplicity that the ferromagnetic NP is

in contact only with the inner shell of CNT and the coupling propagates along this one inner shell. The conductivity of this shell in defective MWCNTs, as was demonstrated experimentally, could be significant and comparable to the conductivity of the outermost shell [55, 56]. The diameter of the inner shell determines the diameter of the NP and in our calculations was selected as $\varnothing_{CNT}$ = 25nm. The axis *Z* is oriented along the CNT axis. To analyze the decay of the RKKY interaction in the presence of SOI the low frequency component of the oscillations of the normalized spin susceptibility χ along the CNT axis was examined,

$$\chi(z) = \mathrm{si}(2k_+|z|)/2 \pm \mathrm{si}(2k_-|z|) \tag{16}$$

where

$$\mathrm{si}(y) = \int_0^y \frac{\sin t}{t} dt - \frac{\pi}{2}$$

The effective wave vectors k_+ and k_- are defined within the model [13] and depend on the diameter of the CNT, its chirality, parameters of the SOI and μ. For certain combinations of these parameters the exchange coupling is long-range and propagates over hundreds of nanometers [13].

Within this approach, we calculated χ looking for a value of the shift of the Fermi level μ due to SOI, which would lead to the decay length of the order of hundreds of nanometers. It should be noted that μ was the only completely free adjustable parameter. The obtained result is presented in Figure 8a, in which we plot the amplitude envelope of the spin susceptibility oscillations along the *z*-axis for μ = 25 meV. Other parameters used in these calculations are as follows. Chiral indices were chosen as (235,129). These values correspond to the $\varnothing_{CNT}$ = 25nm. The angle of chirality in this case is equal to 39.54° and the circumferential direction k_G = 0.053 nm^{-1}. The constant of spin-orbit splitting Δ_{SO} following data of other authors, was chosen to be equal to 6 meV [13, 51]. Finally, the period of oscillations of spin susceptibility for this set of parameters is of the order of 0.5 nm, this result is shown in Figure 8b.

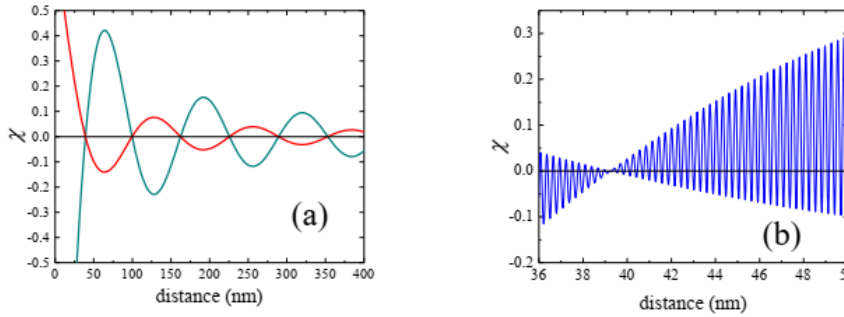

Figure 8. (a) Envelope of the spin susceptibility amplitude oscillations along the CNT axis; (b) High frequency oscillations of the spin susceptibility in the real space.

The obtained chiral indices emphasize the fact that the curvature effects are rather negligible, as should be in a purely theoretical case for a SWCNT of such large diameter. It follows from the result of Figure 8 that for the considered parameters of the nanotube the IEC could propagate on hundreds of nanometers. Even if this result can be regarded only as an indication that the long-range interaction can really occur in our samples, it strongly supports the idea that the IEC directly affects the coupling between ferromagnetic NPs via the CNT medium as was clearly derived from the elaboration of the $M(H)$ data. To make this statement more solid, it is necessary to carry out the calculations for multi-walled CNT. In addition, the external magnetic field strengthens the SOI and, consequently, could intensify the exchange coupling at large distances.

IMPACT OF THE MAGNETIC ANISOTROPY ON THE RELAXATION OF THE MAGNETIC MOMENTS IN FCCVD SAMPLES

Samples studied in this research have been synthesized by FCCVD with high ferrocene concentration, C_F = 10 wt.%. In this case ferromagnetic NPs are localized almost uniformly throughout the sample, i.e., inside and outside CNTs, see Figure 9. The interparticle interaction

can be described well within the RAM [14, 16]. Local magnetic moments of single domain NPs are oriented randomly and the exchange interaction between them exceeds the gain in energy due to magnetic anisotropy. Correlations of the magnetic anisotropy axes decay rapidly on a short range, order of the NP size, see Eq. (12). In the light of these results, it is interesting to study the influence of the distribution of orientations of the local magnetization vectors and of the magnetic anisotropy induced barriers between metastable magnetic states on the relaxation processes. This is one of the key points in understanding the mechanisms of interaction of alternating magnetic field with a CNT-based magnetic nanocomposite.

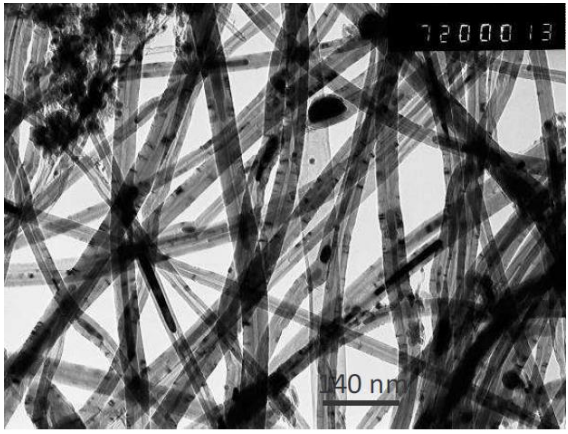

Figure 9. TEM image of CNT-based nanocomposite synthesized with C_F = 10 wt.%.

The main phase of the NP material is cementite Fe_3C [14, 57]. Detailed information regarding the structure of carbon matrix can be obtained from Raman spectroscopy. Typical Raman spectrum of studied CNT is presented in Figure 10. The spectrum is dominated by three pronounced bands: one non dispersive band G centered at ~1580 cm^{-1}, and two dispersive bands, D and 2D. In our experiment D and 2D bands are centered at ~1350 cm^{-1} and ~2700 cm^{-1}, respectively. G band is associated with the in plane E_{2g} optical modes, whereas 2D band comes from TO modes and involves two phonons (second order process). Contrary to its

second order overtone 2D band, which is always Raman active, D-band requires the presence of defects for its activation [58]. Thus, the intensity of D band is generally accepted as an indicator of defect amount in graphitic systems. Besides, the crystalline size, L_a, can be evaluated from the intensity ratio I_D/I_G [59]. In the case of our sample we get $L_a \sim 32$ nm. In its turn, the intensity of 2D band is proportional to long range order in MWCNT [60]. Moreover, several minor (in terms of intensity) bands are observed in the spectra. The positions of these bands centered at appx. 1100 cm^{-1}, 1470 cm^{-1}, 1620 cm^{-1}, 2450 cm^{-1} and 2900 cm^{-1}, denoted in the plot as D'', D_3, D', D+D'', D+D', respectively. However, the assignment of these peaks is not unambiguous and different interpretation can be found in the literature. For example, the low frequency shoulder of D band which appears at appx. 1100 – 1200 cm^{-1} is often denoted by D_4 [61]. On the other hand, assignment of D+D' to D+G mode [62] also can be found in the literature. The detailed overview of Raman spectroscopy of carbon-based materials with related references can be found elsewhere [63], we only would like to emphasize here that the presence of D_3 and D_4 is the sign of the presence of amorphous carbon and hydrocarbons built-in graphitic matrix [61].

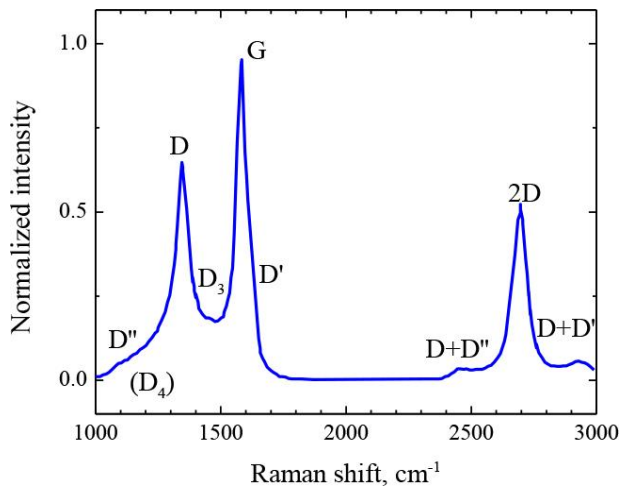

Figure 10. The Raman spectra of synthesized CNTs. The alternative assignment is in the brackets (see the text).

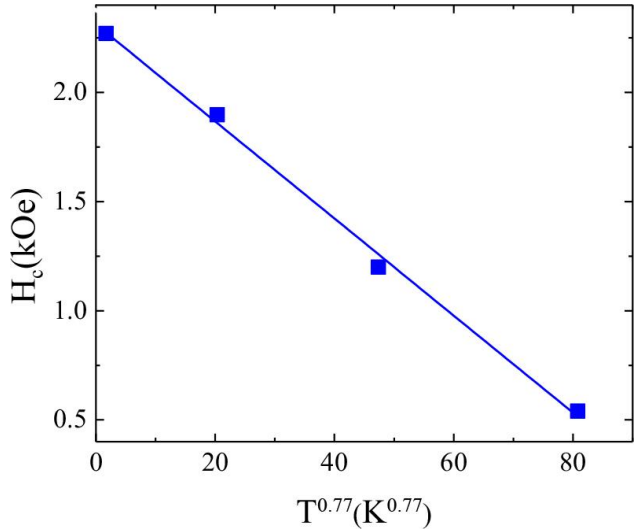

Figure 11. Coercivity versus temperature (2 K < T < 300 K). Solid line is the best linear fit.

Magnetic hysteresis loops were measured for this sample in the temperature range 2 – 300 K. Data were similar to the previously reported in [14, 15]. The coercivity fields H_C were extracted from these measurement. Their values vary in the range from 0.5 to 2.2 kOe, which is much greater than those usually reported for bulk Fe_3C [64]. We believe that this is a clear indication of small size effects on the H_C values, i.e., the coercivity of single domain NP is usually much greater than those of bulk [1]. For this case and for the intermediate temperatures H_C is expected to follow the law expressed in Eq. (17):

$$H_C(T) = H_C(0)\left[1 - (T/T_B)^{\zeta}\right], \tag{17}$$

where T_B is blocking temperature of the largest particles and exponent ζ depends on the alignment of the local magnetic moments of particles [1]. In particular, for random orientation ζ = 0.77 [65]. In Figure 11 we show the H_c versus $T^{0.77}$ dependence. The solid line represents the best linear fit. The result of Figure 11 confirms the random distribution of local magnetic moments. Moreover, we have also estimated the blocking temperature of

the largest particles: T_B is close to T = 415 K. This value is smaller than the Curie temperature of cementite, 481 K.

From the above analysis we may conclude that studied CNT-based nanocomposite should be characterized by random magnetic anisotropy. Such systems are well described within the RAM [42]. The LAS can provide in this case a valuable information about the dimensionality of the system, correlations of magnetic anisotropy axes [32, 33, 46, 47] and the dominant role of the interparticle interaction [14, 35]. For all temperatures, the best fit to the $M(H)$ data was given by the $H^{-1/2}$ law (Figure 12), which corresponds to the 3D exchange coupled system.

The correlation function of the magnetic anisotropy axes was desribed by the Eq. (12). In Figure 13 we show measured $M(H)$ dependences along with the results of the best fit procedure according to Eq. (2). The term of the coherent anisotropy was absent in this case. The exchange field was 2.9 kOe for the whole T range while the H_{ra} varies between 5.4 kOe (T = 2 K) and 3.2 kOe (T = 300 K).

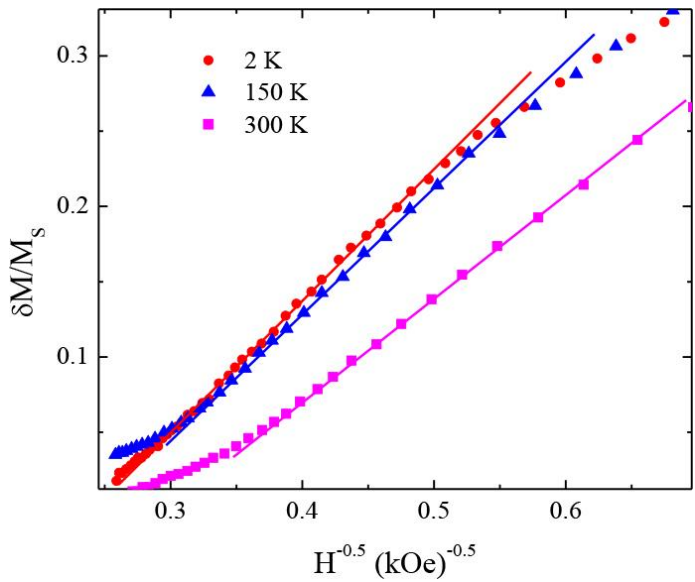

Figure 12. Approaching to magnetic saturation in the temperature range 2 K–300 K for CNT-based magnetic nanocomposite synthesized by FCCVD with C_F = 10 wt.% of ferrocene.

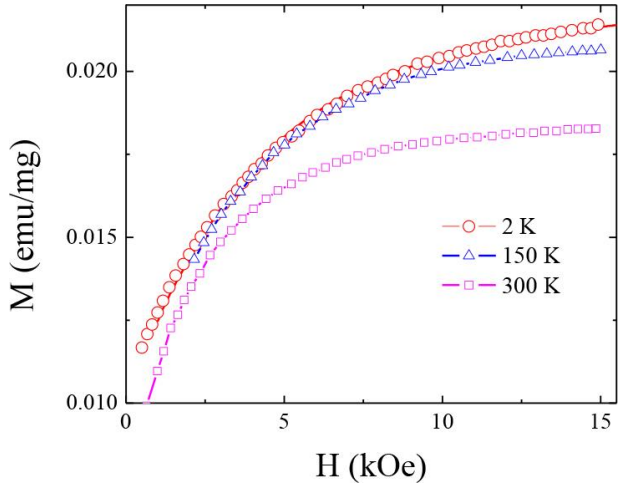

Figure 13. Measured (symbols) and calculated (lines) $M(H)$ dependences for T = 2, 150 and 300 K.

On this sample we performed the magnetic relaxation measurements. It was first saturated at H = 15 kOe and after we did change the magnetic field to the value of -50 Oe, i.e., it was applied in the opposite direction. Instead of simply remove the magnetic field to zero, the presence of this negative small magnetic field pretends to compensate the possible magnetic remanence of the SQUID magnetometer. This experiment was done in a wide range of temperatures (from 2 K to 300 K) and the magnetization was measured as a function of time. As described in Eq. (18) [66-68] during the relaxation process the magnetization decays in a logarithmic way with time. By studying the slope in this process (i.e., the demagnetization velocity) the characteristic magnetic viscosity (S) can be determined,

$$M(t) = M(t_0)\left[1 - S(T,H)\ln\left(\frac{t}{t_0}\right)\right] \quad (18)$$

where t_0 is the inverse of the attempt frequency. Figure 14a shows the S values calculated for each one of the different temperatures at which measurements were performed. There is a nonlinear increasing tendency of S with respect to temperature which reflects the distribution of the barriers

for magnetic anisotropy between various metastable magnetic states. The obtained $S(T)$ dependence makes it possible to restore the distribution function of the magnetic nanoparticles $f(V)$ in the volume V, which is related to the magnitude of the potential barrier in the relaxation of the magnetization. According to the model of slow relaxation at $H<<H_{ra}$ the magnetic viscosity $S(T,t)$ is expressed as [66-68]

$$S(T,t) = \frac{kTV_B f(V_B)}{K(T)\langle V\rangle \int_0^\infty f(V)dV}, \tag{19}$$

where k is the Boltzmann constant, $K(T)$ is the temperature dependent anisotropy constant, V_B is the volume of NPs which effectively contribute to the relaxation, $V_B = \frac{kT}{K(T)} ln(t/t_0)$ and $\langle V\rangle = \frac{\int_0^\infty f(V)VdV}{\int_0^\infty f(V)dV}$.

The analysis of Eq. (19), considering the obtained $S(T)$ dependence, Figure 14a, showed that the distribution function can be represented in the form

$$f(V) = \frac{1}{V} exp\left[-\varphi(T)\frac{V}{V_0}\right], \tag{20}$$

where $\varphi(T)$ is a test function that depends only on temperature, $V_0 = kT_B \ln\left(\frac{t}{t_0}\right)/K_B$ and K_B is the anisotropy constant at $T = T_B$. The presence of the function $\varphi(T)$ is explained by the fact that the parameters affecting the magnetic viscosity (such as the anisotropy constant, the saturation magnetization) depend on temperature in the considered temperature range. In addition, the experimental dependence $S(T)$ is essentially non-linear.

Substituting Eq. (20) into Eq. (19), taking into account that the quantity $\langle V\rangle \int_0^\infty f(V)dV = V_0/\varphi(T)$, we obtain the transcendental equation for the function $\varphi(T)$

$$S(T,t)\ln\left(\frac{t}{t_0}\right) = \varphi(T)\frac{T}{T_B}\frac{K_B}{K(T)} exp\left[-\varphi(T)\frac{T}{T_B}\frac{K_B}{K(T)}\right] \tag{21}$$

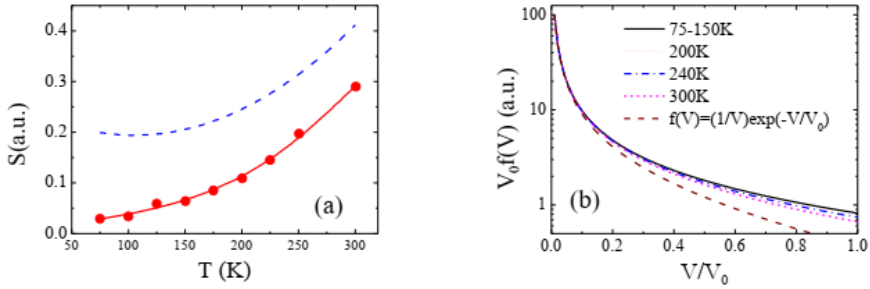

Figure 14. (a) Magnetic viscosity versus temperature with a reverse magnetic field applied of 50 Oe after the saturation (points). Dashed and solid lines correspond to the test function $\varphi(T)$ and $S(T)\ln(t/t_0)$ dependences, respectively; (b) The normalized distribution function $f(V)$ as obtained at different temperatures. Dashed line is for $f(V) = (1/V)\exp(-V/V_0)$ distribution function.

The temperature dependent anisotropy constant can be evaluated from RAM [16, 32]

$$[K(T)]^2 = \frac{H_c(T)A^3M_S(T)}{114(kT_B)^2}, \tag{22}$$

where A is the exchange constant, the coercive force H_C is defined by the Eq. (17). Considering both the $H_C(T)$ at $T < T_B$ (Figure 11) and the $M_s(T)$ (the Bloch law) dependencies for the considered sample [14], we arrive to the expression

$$S(T,t)\ln\left(\frac{t}{t_0}\right) = F(T)exp(-F(T)) \tag{23}$$

where function

$$F(T)=\gamma_0\varphi(T)\gamma(T), \tag{24}$$

and

$$\gamma(T) = \frac{T}{T_B}\left\{\left[1-\left(\frac{T}{T_B}\right)^{0.77}\right]\left(1-BT^{3/2}\right)\right\}^{-1/2} \tag{25}$$

In. Eq. (25) B is the Bloch constant, and γ_0 is

$$\gamma_0 = \frac{\sqrt{114}K_B(kT_B)}{\left(H_C^0 A^3 M_S^0\right)^{1/2}}, \tag{26}$$

where H_C^0 and M_S^0 are the coercivity and saturation magnetization, respectively, at $T = 0$.

With Eq. (23) on the base of the obtained $S(T)$ dependence (Figure 14a) and assuming that $\ln(t/t_0) = 25$, we first find the function $F(T)$. Afterwards, within the Eq. (24) we extract the test function $\varphi(T)$, which after the subsequent approximation can be represented as a polynomial of the second degree

$$\varphi(T) = a + bT + cT^2 \tag{27}$$

For the considered case $a = 0.258$, $b = -1.216 \times 10^{-3}$ K^{-1} and $c = 5.755 \times 10^{-6}$ K^{-2}.

To fit the $S(T)$ dependence we used the previously obtained parameters for such samples as well as measured in this work, $A = (3\text{-}5)\times10^{-12}$ J/m, $M_S^0 = (1.26\text{-}1.33)\times10^6$ A/m, $K_B = 10^4$ J/m^3, $B = 1.65\times10^{-5}$ K$^{-3/2}$ [14, 15, 32], $H_C^0 = 2.132$ kOe, $T_B = 415$ K (Figure 11).

The obtained test function $\varphi(T)$ and $S(T)\ln(t/t_0)$ dependences are shown in Figure 14a by dashed and solid lines, respectively. As it follows from this result, a good agreement with the experiment is reached confirming the proposed hypothesis about the distribution function as given in Eq. (20).

It follows from Figure 14a that the test function $\varphi(T)$ in the range 75 – 150 K is temperature independent, whereas the magnetic viscosity $S(T)$ times $\ln(t/t_0)$ is determined by $F(T)$. It means that the $S(T)$ dependence is determined only by $\gamma(T)$, in which the linear increase is modified by the temperature dependence of the anisotropy constant. That is, in the temperature range 75–150 K the linear dependence of the magnetic viscosity is modified by the temperature dependence of the anisotropy constant $K(T)$. This suggests that in this T range the relaxation process is mainly determined by the anisotropy of the sample. In the range 150–300

K the effect of the test function $\varphi(T)$ is manifested. Its influence leads to correction of the function $F(T)$ in the direction of the increase with respect to $\gamma(T)$.

We would like to underline, that in the entire temperature range the magnetic viscosity with high accuracy can be expressed by the expansion

$$S(T)\ln(t/t_0) = F(T)[1-F(T)+(1/2)F^2(T)], \quad (28)$$

in which terms in square brackets contribute to the region $T > 150$ K. The approximated expression (28) is very convenient for the experimental data fitting instead of Eq. (23).

In addition, we obtained that, at $T > 150$ K the test function tends to compensate the temperature contribution of the anisotropy constant which leads to the practically linear $S(T)$ dependence within the range 230 – 300 K. This is probably because in this temperature range the magnetic viscosity becomes independent on the variation of the anisotropy constant. In other words, with an increase in temperature, when the anisotropy constant decreases and the contribution of thermal fluctuations increases, the relaxation mechanism ceases to react to the anisotropy change.

In Figure 14b we show the distribution function $f(V)$ at different temperatures obtained using the calculated test function $\varphi(T)$. Data are restricted to the region $V < V_0$, which means that the temperature is well below blocking. This is a necessary condition for the application of the slow relaxation model [67]. It follows from Figure 14b that the distribution function is practically independent on temperature. Only for $T = 300$ K the values of the distribution function differ from the values at lower temperatures, when the volume V tends to V_0. This could reflect the fact that at $T = 300$ K we are too close to the blocking temperature and the applicability of the model begins to experience limitations.

The test function $\varphi(T)$ is an important factor in the successful fitting of the magnetic viscosity data. Without this function, the distribution function becomes equal to $(1/V)\exp(-V/V_0)$. With this function we failed to fit the experimental data. In Figure 14b, for comparison, by dashed line we plot

the $f(V) = (1/V) \exp(-V/V_0)$ distribution function. It can be seen that it differs from that obtained, especially with increasing volume.

IMPACT OF MAGNETIC ANISOTROPY ON THE MAGNETIC ISOLATION OF CLOSELY PACKED CO NANOPARTICLES EMBEDDED IN CNT GROWN BY PECVD

It is now well known that in order to form a densely packed array of ferromagnetic NPs, prevent their agglomeration and achieve long-time protection against external environment, one of the best ways is to embed them into the carbon nanotubes (CNTs) [69-72]. Selective introducing into the inner channel of multiwalled CNTs could give rise to a new family of hybrid materials with novel functionality which can find applications in magnetoelectronics. The dipole-dipole interaction (DDI) usually dominates for the density of nanosized ferromagnets greater than $n_{NP} \approx 10^9 – 10^{10}$ cm^{-2} [73]. Therefore, to create a system of densely packed magnetically isolated ferromagnetic nanoparticles with $n_{NP} > 10^{10}$ cm^{-2}, it is necessary to increase the contribution of the magnetic anisotropy in the total energy of the system.

Figure 15a presents the MFM image for the reference sample, and Figure 15b shows the MFM result for an array of CNTs with Co on the top of each CNT. The intensity variations are a measurement of the attractive (repulsive) magnetic force gradient.

In the first case, it is possible to distinguish magnetic domains with an average size of about 500 nm encompassing a set of many NPs, which indicates strong DDI between them. For Co-CNT sample, which was grown from a reference one, the average size of magnetic dipole is about 50 nm, which is close to the average size of Co at the top of the CNT. Thus, Co NPs are magnetically separated from each other.

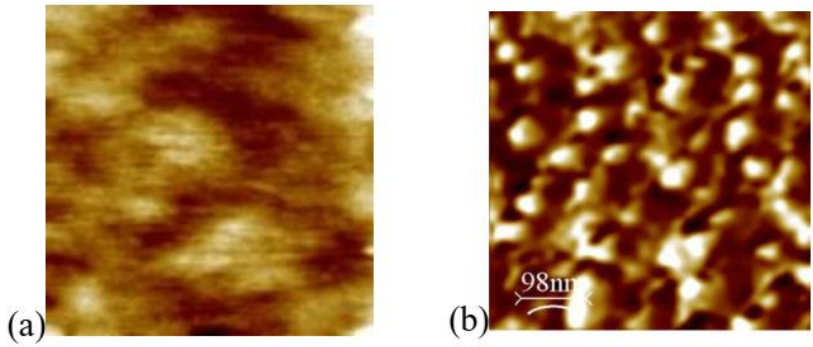

Figure 15. (a) MFM image of Co NPs on SiO_2/Si substrate. The size of image is 1.5 μm × 1.5 μm; (b) MFM image of Co NPs embedded inside CNT.

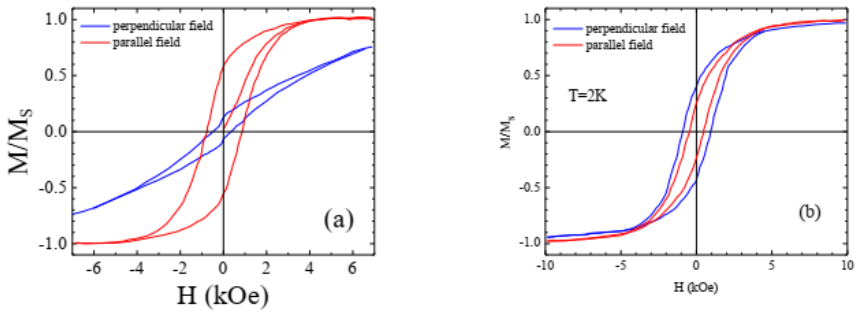

Figure 16. *M*(*H*) curves for the parallel (red color) and perpendicular (blue color) magnetic field orientations. *T* = 2 K. (a) reference sample; (b) Co-CNT.

The difference in the magnetic interaction between the particles on the substrate and inside the CNT is also manifested in the shape of hysteresis loops. In Figure 16a the *M*(*H*) curves for the reference sample is shown for magnetic field oriented both parallel and perpendicular to the substrate. Rapid saturation in the parallel field along with greater values of the remanence and coercivity can be reasonably attributed to an axis of easy magnetization oriented parallel to the substrate. This can be naturally explained by strong DDI between NPs, because of which the array of NPs can be considered as a thin film.

For Co-CNT sample *M*(*H*) loops approach each other for a parallel and perpendicular field directions, see Figure 16b. Usually for an ensemble of Co NPs with the aspect ratio ≥ 3-5 the easy axis is oriented along the

cylinder and $M(H)$ shapes for the easy and hard axes directions differ significantly [74]. Therefore, most likely, in our Co-CNT samples there is a complex case where magnetocrystalline and, possibly, magnetoelastic anisotropy of NPs have a dispersion relative to some direction at a certain angle to the axis of the nanocylinders. This fact leads to uncertainty in the direction of the axis of easy magnetization, which requires additional analysis.

We start again from the RAM, the validity of which for CNT-based nanocomposites was shown in previous sections of this chapter. The effective magnetic anisotropy constant K which includes contributions of the magnetocrystalline and shape anisotropies, the magnetoelastic contribution and the DDI (K_{DD}), can be evaluated within the random anisotropy model, which has been successfully applied in the past to explain the properties of ferromagnetic NPs in CNT [32],

$$H_C = 114K^2(kT_B)^2/(A^3M_S). \quad (29)$$

Below the results will be presented for the parallel field. For the perpendicular field the data are similar. The T_B (400 K), H_C (6.53×10^4 A/m for reference sample and 3.76×10^4 A/m for Co-CNT) and M_S (1.4×10^6 A/m) were measured. For nanosized Co we took from literature $A = 1.54 \times 10^{-11}$ J/m [75]. Thus, for the reference sample $K = 3.77 \times 10^5$ J/m^3 and for Co-CNT sample $K = 2.65 \times 10^5$ J/m^3.

The contribution of the DDI is expressed as [76]

$$K_{DD} = (1/8\pi)(\mu_0 M_S^2 V_{NP}/\zeta^3)s_d, \quad (30)$$

where ζ is an average interparticle distance, $s_d = 6 – 8$ is a lattice sum that depends on the type of lattice in the NPs arrangement and the dimensionality of the sample, V_{NP} is the NP volume and μ_0 is magnetic permeability of vacuum. From Eq. (30) we estimate $K_{DD} = 1.4\times10^5$ J/m^3 for the reference sample and $K_{DD} = 1.1 \times 10^5$ J/m^3 for the Co-CNT. The contribution of the SA for the reference sample can be neglected due to the

almost equal transverse and longitudinal demagnetizing factors. In addition, we believe that the contribution of the magnetoelastic anisotropy will be unimportant because the Co nanoparticles are in a practically free state.

Therefore, the anisotropy constant K for the reference sample is a function of only K_{DD} and K_{MC}. This results in $K_{MC} = 2.4\times10^5$ J/m^3. This value is assumed to be the same for both types of samples. The obtained K_{MC} is slightly greater that K_{DD}. Nevertheless, the impact of the DDI in the presence of only of MCA is determined by the dipolar coupling constant $\alpha_D = K_{DD}/K_{MCA}$ [77]. There is a crucial parameter α_{cr} that determines the transition from a single particle to the collective behavior. The reported values for *fcc* or *hcp* Co NPs are α_{cr}= (0.2−0.4)$(d_n/\zeta)^3$ [78]. If $\alpha_D > \alpha_{cr}$, then DDI dominates, otherwise the MCA prevails. For our ensemble of Co NPs we get $\alpha_{cr} \approx 0.14 < \alpha_D = 0.58$, which indicates that the energy contribution of the DDI is sufficient to form regions covering many NPs, that is indeed observed experimentally.

For the Co-CNT sample, the contribution of the SA and MEA is important. Anisotropy constants K_{SA} and K_{DD} of the system of magnetic nanocylinders can be merged in a single contribution as [79]

$$K_{SA} + K_{DD} = -(1/4)\mu_0 M_S^2(1 - 3P). \quad (31)$$

Here $P = (\pi r^2 S)$ is the porosity of Co nanowires assembly, $P = 0.06$. From Eq. (31) we get $K_{SA}+K_{DD} = -5.1\times10^5$ J/m^3, which leads to $K_{SA} = -6.2 \times 10^5$ J/m^3. Finally, on the base of the above estimations we calculate the value of the magnetoelastic anisotropy constant, $K_{ME} = 5.4 \times 10^5$ J/m^3. This energy density is greater than those reported in literature for Co nanowires embedded in porous matrix [80]. In Table 1 we present the results of the evaluations of the SA, MCA and DDI for both samples for the parallel field. We do not show K_{ME} in this Table. The discussion of this issue will be done further.

Table 1. Evaluations of the SA, MCA and DDI for the parallel orientation of the magnetic field. d_n is an average diameter of the NP and L is an average height of the nanocylinder

Parameter	Unit	Reference sample	Co-CNT
K_{SA}	J/m^3	---	-6.16 × 10^5
K_{DD}	J/m^3	1.4 × 10^5	1.09 × 10^5
K_{MC}	J/m^3	2.37 × 10^5	2.37 × 10^5
$K_{SA}+K_{DD}$	J/m^3	---	-5.07 × 10^5
$\alpha_D = K_{DD}/K_{MC}$	a.u.	0.61	---
ζ	nm	32.6	51.5
S	cm^{-2}	3 × 10^{10}	1.2 × 10^{10}
P	a.u.	0.15	0.06
d_n	nm	25 ± 8	15 ± 5
L	nm	---	100-150

For the Co-CNT array we have to consider both the SA and MEA. Their contribution along with the MCA should exceed the contribution of the dipole interaction between NPs.

The type of Co crystalline lattice affects significantly the interpretation of data on the magnetoelastic anisotropy. For *fcc* Co the K_{ME} can be evaluated as

$$K_{ME}^{fcc} \approx -(3/2)\lambda\sigma, \tag{32}$$

where λ is the magnetostriction constant and σ is the elastic stress. Using for *fcc* Co λ = –50×10^{-6} [81] and applying the obtained K_{ME} value we estimate σ ≈ 7.13 GPa.

For *hcp* Co when the hexagonal axis is parallel to the CNT axis, the K_{ME} is expressed as [82]

$$K_{ME}^{hcp} = \sigma(\lambda_A + \lambda_B)\varepsilon_1, \tag{33}$$

where λ_A and λ_B are magnetostriction constants and ε_1 is strain. From Eq. (33) we get the tensile stress σ ≈ 3.4 GPa.

For the hexagonal axis oriented perpendicular to the CNT axis the situation changes significantly. The expression for the K_{ME}^{hcp} depends on the orientation of the crystal magnetization $\vec{m}$ [81]. However, the exact values of the direction cosines α_i of $\vec{m}$ with respect to the hexagonal axis are not known in our case. Therefore, for random α_i

$$K_{MEA}^{hcp}(\vec{m}) \approx B_2\varepsilon_3 + B_3(\varepsilon_1 + \varepsilon_2), \tag{34}$$

where B_i are magnetoelastic coupling coefficients, the indices number the axes of the hexagonal crystal (index 3 corresponds to the hexagonal axis *c*, indices 1 and 2 correspond to the *a* and *b* axes, respectively). We used $B_2 = -29 \times 10^6$ J/m^3, $B_3 = 28.2 \times 10^6$ J/m^3 [81]. The strain ε is found from the system of equations

$$c_{ij}\varepsilon_j = \sigma_i, \tag{35}$$

where c_{ij} are elastic stiffness constants, $\sigma_1 = \sigma_3 = \sigma$ and $\sigma_2 = 0$. For the considered case we evaluate $\sigma = -9.5$ GPa. Such internal elastic stresses cause the strain of the CNTs lattice not more than $\varepsilon \approx 10^{-3}$, which is in good agreement with the literature [83].

The performed evaluations show that the DDI is suppressed mainly by the SA and MEA. The largest contribution of the magnetoelastic anisotropy occurs when the hexagonal axis is oriented parallel to the substrate. This is confirmed by the results of micromagnetic simulation, which was performed for *hcp* Co nanocylinders with diameter 20 nm and length 100 nm. We applied the Nmag package [84] based on the Landau-Lifshitz-Gilbert equation.

Axis *Z* is oriented along the nanocylinder axis (i.e., the CNT orientation), and *XY* plane is lying in the radial direction. The *X* axis coincides with the hexagonal axis of the *hcp* Co. The simulation shows that under such conditions the relaxed magnetization configuration of the cylinder depends on the K_{ME}, Figure 17. For $K_{ME} = 0$, the magnetization of the Co nanocylinder is homogeneous and oriented along the *Z* axis, Figure

17a. The presence of the magnetoelastic stresses, $K_{ME} = 5.35 \times 10^5$ J/m^3, breaks nanocylinder on two domains, Figure 17b.

The performed simulations of the magnetic structure of Co nanocylinders should be considered only as evaluation results showing that with the magnetoelastic component nanocylinders may be partitioned into domains, which leads to a decrease in remanence and coercivity and to isotropy of the magnetic properties. This is in good agreement with the experimental data.

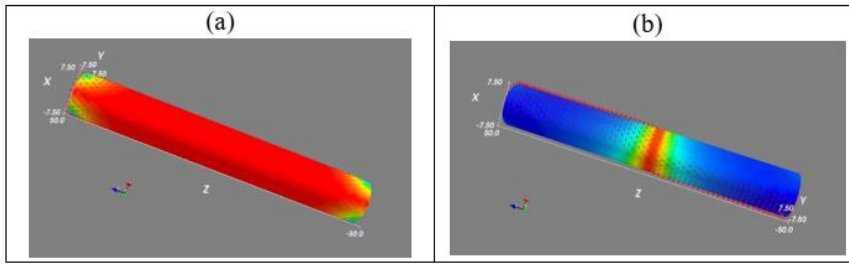

Figure 17. Relaxed magnetization configuration of *hcp* Co nanocylinder of diameter 20 nm and length 100 nm for the absence of stress, $K_{ME} = 0$ (a) and $K_{ME} = 5.35 \times 10^5$ J/m^3(b). Red color corresponds to the magnetization direction along the nanocylinder axis, blue color corresponds to the magnetization direction oriented perpendicular to the nanocylinder axis.

CONCLUSION

In this chapter we have presented different magnetic characteristics of CNT-based magnetic nanocomposites grown by CVD. Carbon nanotubes were vertically aligned. The arrangement of single domain ferromagnetic nanoparticles varied from one nanoparticle in each nanotube to several spaced nanoparticles localized within inner CNT channel and, finally, to an arbitrary distribution of nanoparticles throughout the sample array. The in-plane packing density of NPs was determined by the density of CNTs and was equal to appx. 10^{10}-10^{11} cm^{-2}. In all these samples magnetic properties were investigated paying special attention to the impact of the magnetic anisotropy. It was obtained that,

- for samples with one NP in each CNT the contribution of the magnetic anisotropy suppresses the magnetostatic dipole interaction between closely packed ferromagnetic NPs leading to the magnetic isolation of NPs;
- for samples with few NPs inside inner CNT channel the coherent magnetic anisotropy is of great importance causing microscopically large coherence of the local magnetic moments. These correlations could propagate up to micrometers. The RKKY interaction via the inner shell of CNTs could enforce this coherence;
- for samples with distributed NP`s arrangement through the whole sample the relaxation of the magnetic moments occurs via different metastable states. The magnetic anisotropy determines the temperature dependence of the magnetic viscosity in the intermediate temperature range.

ACKNOWLEDGMENTS

S. L. Prischepa and I. V. Komissarov acknowledge the financial support of the “Improving of the Competitiveness” Program of the National Research Nuclear University MEPhI – Moscow Engineering Physics Institute. The authors would like to thank F. Le Normand, J. Tejada and A. V. Kukharev for valuable discussions and suggestions.

REFERENCES

[1] Dorman, J. L., Fiorani, D. and Tronc, E. (1997). Magnetic relaxation in fine-particle systems. *Adv. Chem. Phys.*, 98: 283-494.

[2] Gubin, S. P., Koksharov, Y. A., Khomutov, G. B. and Yurkov, G. Yu. (2005). Magnetic nanoparticles: preparation, structure and properties. *Russ. Chem. Rev.*, 74 (6): 489-520.

[3] Proctor, T. C., Chudnovsky, E. M. and Garanin, D. A. (2015). Scaling of coercivity in a 3d random anisotropy model. *J. Magn. Magn. Mater.*, 384: 181-185.

[4] Liu, J., Qiao, S. Z., Hu, Q. H. and Lu, G. Q. (Max) (2011). Magnetic nanocomposites with mesoporous structures: synthesis and applications. *Small*, 7 (4): 425-443.

[5] Faupel, F., Zaporojtchenko, V., Strunkus, T. and Elbahri, M. (2010). Metal-polymer nanocomposites for functional applications. *Adv. Eng. Mater.*, 12 (12): 1177-1190.

[6] Wildgoose, J. J., Banks, C. E. and Compton, R. G. (2006). Metal nanoparticles and related materials supported on carbon nanotubes: methods and applications. *Small*, 2 (2): 182-193.

[7] Jourdain, V. and Bihara, C. (2013). Current understanding of the growth of carbon nanotubes in catalytic chemical vapor deposition. *Carbon*, 58: 2-39.

[8] Vorobjova, A. I., Shimanovich, D. L., Yanushkevich, K. I., Prischepa, S. L. and Outkina, E. A. (2016). Properties of Ni and Ni-Fe nanowires electrochemically deposited into a porous alumina template. *Beilstein J. Nanotechnol*., 7: 1709-1717.

[9] Labunov, V. A., Danilyuk, A. L., Prudnikava, A. L., Komissarov, I. V., Shulitski, B. G., Speisser, C., Antoni, F., Le Normand, F. and Prischepa, S. L. (2012). Microwave absorption in nanocomposite material of magnetically functionalized carbon nanotubes. *J. Appl. Phys*., 112 (2): 024302(1-9).

[10] Costa Jr., A. T., Kirwan, D. F. and Ferreira, M. S. (2005). Indirect exchange coupling between magnetic adatoms in carbon nanotubes. *Phys. Rev. B*, 72 (8): 085402(1-8).

[11] He, J., Zhou, P., Jiao, N., Ma, S. Y., Zhang, K. W., Wang, R. Z. and Sun, L. Z. (2014). Magnetic exchange coupling and anisotropy of 3d transition metal nanowires on graphyne. *Sci. Rep*., 4: 4014(1-9).

[12] Costa, A. T., Rocha, C. G. and Ferreira, M. S. (2007). Noncollinear coupling between magnetic adatoms in carbon nanotubes. *Phys. Rev. B*, 76 (8): 085401(1-5).

[13] Klinovaja, J. and Loss, D. (2013). RKKY interaction in carbon nanotubes and graphene nanoribbons. *Phys. Rev. B*, 87 (4): 045422(1-11).

[14] Danilyuk, A. L., Prudnikava, A. L., Komissarov, I. V., Yanushkevich, K. I., Derory, A., Le Normand, F., Labunov, V. A. and Prischepa, S. L. (2014). Interplay between exchange interaction and magnetic anisotropy for iron based nanoparticles in aligned carbon nanotube arrays. *Carbon*, 68: 337-345.

[15] Prischepa, S. L., Danilyuk, A. L., Prudnikava, A. L., Komissarov, I. V., Labunov, V. A. and Le Normand, F. (2014). Exchange coupling and magnetic anisotropy for different concentration of iron based nanoparticles in aligned carbon nanotube arrays. *Phys. Status Solidi C*, 99 (5-6): 1074-1079.

[16] Chudnovsky, Eugene M. (1995). In: *The magnetism of amorphous metals and alloys*, edited by Fernandez-Baca, J. A. and Ching, W.-Y. (World Scientific, Singapore) Ch. 3: 143-175.

[17] Komogortsev, S. V., Iskhakov, R. S., Balaev, A. D., Kudashov, A. G., Okotrub, A. V. and Smirnov, S. I. (2007). Magnetic properties of Fe_3C ferromagnetic nanoparticles encapsulated in carbon nanotubes. *Phys. Sol. State*, 49 (4): 734-738.

[18] Varvaro, G., Albertini, F., Agostinelli, E., Casoli, F., Fiorani, D., Laureti, S., Lupo, P., Ranzieri, P., Astinchap, B. and Testa, A. M. (2012). Magnetization reversal mechanism in perpendicular exchanged-coupled Fe/L_{10}-FePt bilayers. *New J. Phys*. 14 (7): 073008(1-14).

[19] Navas, D., Torrejon, J., Béron, F., Redondo, C., Batallan, F., Toperverg, B. P., Devishvili, A., Sierra, B., Castaño, F., Pirota, K. R. and Ross C. A. (2012). Magnetization reversal and exchange bias effects in hard/soft ferromagnetic bilayers with orthogonal anisotropies. *New J. Phys*. 14 (11): 113001(1-21).

[20] Akulov, N. S. (1931). Zur Theorie der Magnetisierungskurve von Einkristallen. *Zeitschr. Physik*. 67 (11-12): 794-807.

[21] Brown Jr., W. T. (1940). Theory of the approach to magnetic saturation. *Phys. Rev*., 58 (8): 736-743.

[22] Fähnle, M. and Kronmüller, H. (1978). The influence of spatially random magnetostatic, magnetocrystalline, magnetostrictive and exchange fluctuations on the law of approach to ferromagnetic saturation of amorphous ferromagnets. *J. Magn. Magn. Mater*., 8 (2): 149-156.

[23] Chudnovsky, E. M. and Serota, R. A. (1983). Phenomenological theory of amorphous magnets with small random anisotropy. *J. Phys. C*, 16 (21): 4181-4190.

[24] Chudnovsky, E. M. (1989). Dependence of the magnetization law on structural disorder in amorphous ferromagnets. *J. Magn. Magn. Mater*., 79 (1): 127-130.

[25] Martínez-Huerta, J. M., de la Torre Medina, J., Piraux, L. and Encinas, A. (2013). Configuration dependent demagnetizing field in assemblies of interacting magnetic particles. *J. Phys.: Condens. Matter*, 25 (22): 226003.

[26] Hiroi, K., Kura, H., Ogawa, T., Takahashi, M. and Sato, T. (2014). Magnetic ordered states induced by interparticle magnetostatic interaction in α-Fe/Au mixed nanoparticle assembly. *J. Phys.: Condens. Matter*, 26 (17): 176001.

[27] Son, Y.-W., Cohen, M. L. and Louie, S. G. (2006) Half-metallic graphene nanoribbons. *Nature (London)*, 444: 347-349.

[28] Lehtinen, P. O., Foster, A. S., Ayuela, A., Krasheninnikov, A., Nordlung, K. and Nieminen, R. M. (2003) Magnetic properties and diffusion adatoms on a graphene sheet. *Phys. Rev. Lett.*, 91 (1): 017202 (1-4).

[29] Giesbers, A. J. M., Uhlirová, K., Konečny, M., Peters, E. C., Burghard, M., Aarts, J. and Flipse, C. F. J. (2013). Interface-induced room-temperature ferromagnetism in hydrogenated epitaxial graphene. *Phys. Rev. Lett.*, 111 (16): 166101(1-5).

[30] Castro, E. V., Peres, N. M. R., Stauber, T. and Silva, N. A. P. (2008). Low-density ferromagnetism in biased bilayer graphene. *Phys. Rev. Lett.*, 100 (18): 186803(1-4).

[31] Pisani L., Montanari, B. and Harrison, N. M. (2008). A defected graphene phase predicted to be a room temperature ferromagnetic semiconductor. *New J. Phys.*, 10 (3): 033002(1-9).

[32] Danilyuk, A. L., Komissarov, I. V., Labunov, V. A., Le Normand, F., Derory, A., Hernandez, J. M., Tejada, J. and Prischepa, S. L. (2015). Manifestation of coherent magnetic anisotropy in a carbon nanotube matrix with low ferromagnetic nanoparticle content. *New J. Phys.*, 17 (2): 023073(1-12).

[33] Chudnovsky, E. M., Saslow, W. M. and Serota, R. A. (1986). Ordering in ferromagnets with random anisotropy. *Phys. Rev. B*, 33 (1): 251-261.

[34] Erdélyi, A. (Editor), (1954). *Tables of Integral Transforms*, 2, (McGraw-Hill Book Co, New York).

[35] Danilyuk, A. L., Komissarov, I. V., Kukharev, A. V., Le Normand, F., Hernandez, J. M., Tejada, J. and Prischepa, S. L. (2017). Impact of CNT medium on the interaction between ferromagnetic nanoparticles. *Europhys. Lett.*, 117: 27007(1-7).

[36] Prischepa, S. L., Danilyuk, A. L., Kukharev, A. V., Le Normand, F. and Cojocaru, C. S. (2019). Self-assembled magnetically isolated Co nanoparticles embedded inside carbon nanotubes. *IEEE Trans. Magn.*, 55: 2300304(1-4).

[37] Cojocaru, C. S. and Le Normand, F. (2006). On the role of activation mode in the plasma- and hot filaments-enhanced catalytic chemical vapour deposition of vertically aligned carbon nanotubes. *Thin Solid Films*, 515: 53-58.

[38] Mane, J. M., Cojocaru, C. S., Barbier, A., Deville, J. P., Thiodjio Sendja, B. and Le Normand, F. (2007). GISAXS study of the alignment of oriented carbon nanotubes grown on plain SiO_2/Si(100) substrates by a catalytically enhanced CVD process. *Phys. Status Solidi A*, 204 (12): 4209-4229.

[39] Le Normand, F., Cojocaru, C. S., Fleaca, C., Li, J. Q., Vincent, P., Pirio, G., Gangloff, L., Nedellec, Y. and Legagneux, P. (2007). A comparative study of the field emission properties of aligned films of

carbon nanostructures, from carbon nanotubes to diamond. *Eur. Phys. J. Appl. Phys.*, 38 (2): 115–127.

[40] Danilyuk, A. L., Kukharev, A. V., Cojocaru, C. S., Le Normand, F. and Prischepa, S. L. (2018). Impact of aligned carbon nanotubes array on the magnetostatic isolation of closely packed ferromagnetic nanoparticles. *Carbon*, 139: 1104-1116.

[41] Chudnovsky, E. M. (1988). Magnetic properties of amorphous ferromagnets. *J. Appl. Phys.*, 64 (10): 5770-5775.

[42] Harris, R., Plischke, M. and Zuckermann, M. J. (1973). New model for amorphous magnetism. *Phys. Rev. Lett.*, 31 (3): 160-162.

[43] Alben, R., Becker, J. J. and Chi, M. C. (1978). Random anisotropy in amorphous ferromagnets. *J. Appl. Phys.*, 49 (3):1653-1658.

[44] Iskhakov, R. S., Komogortsev, S. V., Balaev, A. D. and Chekanova, L. A. (2000). Dimensionality of a system of exchange-coupled grains and magnetic properties of nanocrystalline and amorphous ferromagnets. *JETP Letters*, 72 (6): 304-307.

[45] Ignatchenko, V. A., Iskhakov, R. S., Popov, G. V. (1982). Law of approach of magnetization to saturation in amorphous ferromagnets. *Sov. Phys. JETP*, 55 (5): 879-886.

[46] Tejada, J., Martinez, B., Labarta, A., Grössinger, R., Sassik, H., Vazguez, M. and Hernando, A. (1990). Phenomenological study of the amorphous $Fe_{80}B_{20}$ ferromagnet with small random anisotropy. *Phys Rev B*, 42 (1): 898-905.

[47] Chudnovsky, E. M. and Tejada, J. (1993). Evidence of the extended orientational order in amorphous alloys obtained from magnetic measurements. *Europhys. Lett.*, 23 (7): 517-522.

[48] Löffler, J. F., Meier, J. P., Doudin, B., Ansermet, J.-P. and Wagner, W. (1998). Random and exchange anisotropy in consolidated nanostructures Fe and Ni: role of grain size and trace oxides on the magnetic properties. *Phys Rev B*, 57 (5): 2915-2924.

[49] Prischepa, S. L. and Danilyuk, A. L. (2019). Anisotropic temperature-dependent interaction of ferromagnetic nanoparticles embedded inside CNT. *Int. J. Nanosci.*, 18 (3&4): 1940015(1-4).

[50] Klinovaja, J., Schmidt, M. J., Braunecker, B. and Loss, D. (2011). Helical modes in carbon nanotubes generated by strong electric fields. *Phys. Rev. Lett.*, 106 (15): 156809(1-4).

[51] Min, H., Hill, J. E., Sinitsyn, N. A., Sahu, B. B., Kleinman, L. and MacDonald, A. H. (2006). Intrinsic and Rashba spin-orbit interactions in graphene sheets. *Phys. Rev. B*, 74 (16): 165310(1-5).

[52] Zhou, W., Vavro, J., Nemes, N. M., Fischer, J. E., Borondicks, F., Kamarás, K. and Tanner, D. B. (2005). Charge transfer and Fermi level shift in p-doped single-walled carbon nanotubes. *Phys. Rev. B*, 71 (20): 205423(1-7).

[53] Kim, S., Jo, I., Dillen, D. S., Ferre, D. A., Fallahazad, B., Yao, Z., Banerjee, S. K. and Tutuc, E. (2012). Direct measurement of the Fermi energy in graphene using a double-layer heterostructure. *Phys. Rev. Lett.*, 108 (11): 116404(1-4).

[54] Steele, G. A., Pei, F., Laird, E. A., Jopi, J. M., Meerwaldt, H. B. and Kouwenhoven, L. P. (2013). Large spin-orbit coupling in carbon nanotubes. *Nat. Commun.*, 4 (1): 1573.

[55] Collins, P. G., Arnold, M. S. and Avouris, P. (2001). Engineering carbon nanotubes and nanotube circuits using electrical breakdown. *Science*, 292 (5517): 706-709.

[56] Stetter, A., Vancea, J. and Back, C. H. (2008). Determination of the intershell conductance in a multiwall carbon nanotube. *Appl. Phys. Lett.*, 93 (17): 172103(1-3).

[57] Prudnikava, A. L., Fedotova, J. A., Kasiuk, J. V., Shulitski, B. G. and Labunov, V. A. (2010). Mössbauer spectroscopy investigation of magnetic nanoparticles incorporated into carbon nanotubes obtained by the injection CVD method. *Semiconductor Physics, Quantum Electronics & Optoelectronics*, 13 (2): 125-131.

[58] Ferrari, A. C. and Robertson, J. (2000). Interpretation of Raman spectra of disordered and amorphous carbon. *Phys. Rev. B*, 61 (20): 14095-14107.

[59] Pimenta, M. A., Dresselhaus, G., Dresselhaus, M. S., Cancado, L. G., Jorio, A. and Saito, R. (2007). Studying disorder in graphite-based

systems by Raman spectroscopy. *Phys. Chem. Chem. Phys.*, 9 (11): 1276-1291.

[60] Di Leo, R. A., Landi, B. J. and Raffaelle, R. P. (2007). Purity assessment of multiwalled carbon nanotubes by Raman spectroscopy. *J. Appl. Phys*. 101 (6): 064307.

[61] Pawlyta, M., Rouzaud, J. N. and Duber, S. (2015). Raman microspectroscopy characterization of carbon black: Spectral analysis and structural information. *Carbon*, 84: 479–490.

[62] Saito, A., Hofmann, M., Dresselhaus, G., Jorio, A. and Dresselhaus, M. S. (2011). Raman scattering of graphene and carbon nanotubes. *Adv. Phys.*, 60 (3): 413–550.

[63] Bokobza, L., Bruneel, J.-L. and Michel Couzi, M. and Raman, C. (2015). Spectra of Carbon-Based Materials (from Graphite to Carbon Black) and of Some Silicone Composites. *J. Carbon Research*, 1 (1): 77-94.

[64] Byeon, J. W. and Kwun, S. I. (2003). Magnetic evaluation of microstructures and strength of eutectoid steel. *Materials Transactions*, 44 (10): 2184-2190.

[65] Pfeiffer, H. and Schüppel, W. (1990). Investigation of magnetic properties of barrium ferrite powders by remanence curves. *Phys. Status Solidi A*, 119 (1): 259-269.

[66] Tejada, J. and Zhang, X. (1995). Experiments in quantum magnetic relaxation. *J. Magn. Magn. Mater.*, 140-144 (Part 3): 1815-1818.

[67] Tejada, J. and Chudnovsky, E. M. (1998). *Macroscopic Quantum Tunneling of the Magnetic Moment*. Cambridge University Press.

[68] Tejada, J., Zhang, X. X. and Chudnovsky, E. M. (1993). Quantum relaxation in random magnets. *Phys. Rev. B*, 47 (22): 14977-14987.

[69] Grobert, N., Hsu, W. K., Zhu, Y. Q., Hare, J. P., Kroto, H. W. and Walton, D. R. M. (1999). Enhanced magnetic coercivities in Fe nanowires. *Appl. Phys. Lett.*, 75 (21): 3363-3365.

[70] Leonhardt, A., Ritschel, M., Kozhuharova, R., Graff, A., Mühl, T., Huhle, R., Mönch, I., Elefant, D. and Schneider, S. M. (2003). Synthesis and properties of filled carbon nanotubes. *Diam. Rel. Mater*., 12 (3-7): 790-793.

[71] Baaziz, W., Begin-Colin, S., Pichon, B. P., Florea, I., Ersen, O., Zafeiratos, S., Barbosa, R., Begin, D. and Pham-Huu, C. (2012). High-density monodispersed cobalt nanoparticles filled into multiwalled carbon nanotubes. *Chem. Mater*., 24 (9): 1549-1551.

[72] Ghunaim, R., Eckert, V., Scholz, M., Gellesch, M., Wurmehl, S., Damm, C., Büchner, B., Mertig, M. and Hampel, S. (2018). Carbon nanotube-assisted synthesis of ferromagnetic Heusler nanoparticles of Fe_3Ga (Nano-Gajfenol). *J. Mater. Chem. C*, 6 (5): 1255-1263.

[73] Vázquez, M., Pirota, K., Torrejón, J., Navas, D. and Hernández-Vélez, M. (2005). Magnetic behavior of densely packed hexagonal arrays of Ni nanowires: influence of geometric characteristics. *J. Magn. Magn. Mater.*, 294 (2): 174-181.

[74] Li, C., Wu, Q., Yue, M., Xu, H., Palaka, S., Elkins, K. and Liu, J. P. (2017). Manipulation of morphology and magnetic properties in cobalt nanowires. *AIP Advances*, 7 (5): 056229(1-5).

[75] Girt, E., Huttema, W., Mryasov, O. N., Montoya, E., Kardasz, B., Eyrich, C., Heinrich, B., Dobin, A. Yu. and Karis, O. (2011). A method for measuring exchange stiffness in ferromagnetic films. *J. Appl. Phys*., 109 (7): 07B765(1-3).

[76] Zaluska-Kotur, M. A. and Cieplak M. (1993). Dipole interaction with random anisotropy - a local-mean-field study. *Europhys. Lett*., 23 (2): 85-90.

[77] Russier, V., Petit, C., Legrand, J. and Pileni, M. P. (2000). Collective magnetic properties of cobalt nanocrystals self-assembled in a hexagonal network: Theoretical model supported by experiments. *Phys. Rev. B*, 62 (6): 3910-3916.

[78] Kechrakos D. and Trohidou, K. N. (2008). Dipolar interaction effects in the magnetic and magnetotransport properties of ordered nanoparticle arrays. *J. Nanosci. Nanotechnol.*, 8 (6): 2929-2943.

[79] Vidal, F., Zheng, Y., Schio, P., Bonilla, F. J., Barturen, M., Milano, J., Demaille, D., Fonda, E., de Oliveira, A. J. A. and Etgens, V. H. (2012). Mechanism of localization of the magnetization reversal in 3 nm wide Co nanowires. *Phys. Rev. Lett*., 109 (11): 117205(1-5).

[80] Sánchez-Barriga, J., Lucas, M., Radu, F. Martin, E., Multigner, M., Marin, P., Hernando, A. and Rivero, G. (2009). Interplay between the magnetic anisotropy contributions of cobalt nanowires. *Phys Rev B*, 80 (18): 184424(1-8).

[81] Sander, D. (1999). The correlation between mechanical stress and magnetic anisotropy in ultrathin films. *Rep. Prog. Phys*., 62 (5): 809-858.

[82] Lee, C. H., He, H., Lamelas, F. J., Vavra, W., Uher, C. and Clarke, R. (1990). Magnetic anisotropy in epitaxial Co superlattices. *Phys. Rev. B*, 42 (1): 1066-1069.

[83] Yu, M. F., Lourie, O., Dyer, M. J., Moloni, K., Kelly, T. F. and Ruoff, R. S. (2000). Strength and breaking mechanism of multi-walled carbon nanotubes under tensile load. *Science*, 287 (5453): 637–640.

[84] http://nmag.soton.ac.uk/nmag/.